Kalman Filter-Based Estimation of Surface Conductivity and Surface Variations in Scanning Tunneling Microscopy

Richa Mishra and S. O. Reza Moheimani, *Fellow, IEEE*

***Abstract*— In this article, we present a novel method for decoupling surface electronic properties from topographic surface variations in scanning tunneling microscope (STM). In a conventional STM image, these surface properties are mixed, and separating them is nontrivial. We perform closed-loop system identification to obtain a dynamic model of the STM. We then use this model in conjunction with a Kalman filter (KF) and a disturbance observer to estimate surface conductivity, σ, and surface variations, h, from the measurements obtained during a scan. We experimentally verify this method by first performing hydrogen depassivation lithography on a Si(100) − 2 × 1 : H passivated surface to demonstrate the effectiveness of our proposed method in accurately estimating surface conductivity and surface height variations.**

***Index Terms*— Hydrogen depassivation lithography (HDL), Kalman filter (KF) estimation, parameter estimation, state-space modeling, surface conductivity (σ), surface variations (h).**

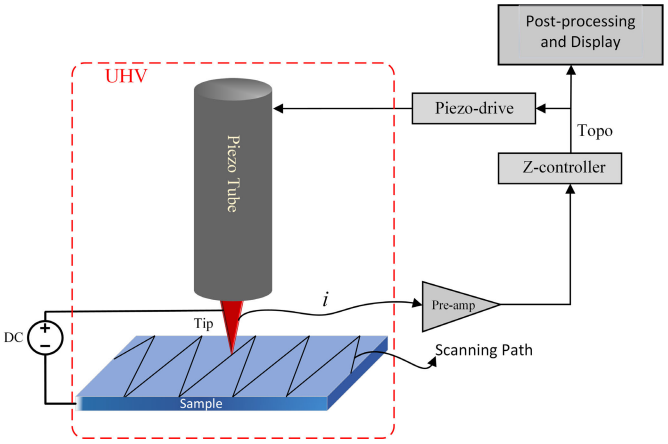

Fig. 1. Schematic of STM operating in constant-current mode. The tip follows a raster pattern to scan the sample. The tip and sample is placed in a UHV.

I. Introduction

A. Working Principle of the STM

DEVELOPMENT of the scanning tunneling microscope (STM) significantly advanced the field of surface science, providing unprecedented resolution at the atomic scale [1], [2]. Owing to its exceptional spatial resolution, the STM has become an indispensable tool for investigating surface topography (imaging) [3], [4], manipulating the atomic structure of surfaces (lithography) [5], [6], [7], and gaining insight on surface electronic properties (spectroscopy) [8]. Much of our understanding of the behavior of matter at the atomic scale is due to the STM, making it a cornerstone of modern surface science [9], [10].

The STM operates by bringing a sharp tip close to a conductive surface and establishing a current between the two objects due to the quantum mechanical phenomenon known as tunneling [2], [11], [12]. The STM utilizes this phenomenon to image the surface with atomic resolution. The distance between the tip and the surface is typically within a few angstroms, and a bias voltage is applied between the probe tip and the surface. This voltage causes electrons to tunnel across the gap. The probability of tunneling decreases exponentially as the distance between the two surfaces increases. By applying a positive voltage to the sample, electrons can tunnel from the tip's occupied states to the sample's unoccupied states and vice versa [8].

The primary mode of STM scanning is the constant-current mode [13], as shown in Fig. 1. During a scan, the tunneling current changes due to features such as variations in surface topography or electronic structure. A feedback controller maintains a constant tunneling current as the tip is scanned across the surface by adjusting the tip–surface distance. The control signal is plotted against the tip position to obtain a 3-D surface topography [11], [14], [15].

However, the resulting topography or controller output does not necessarily represent the true topography of a surface since, during a scan, the controller reacts to variations in surface conductivity as well as surface variations. Variations in surface conductivity are due to variations in the energy barrier for tunneling electrons. A lower energy barrier means more electrons can tunnel through, which means higher conductivity and a higher tunneling current. Therefore, the controller retracts the tip to maintain the set-point current [16]. Consequently, the STM topography image combines surface variations and surface electronic features that are difficult to separate.

Manuscript received 20 November 2023; accepted 14 January 2024. This work was supported by the United States Department of Energy under Award DE-EE0008322 and Award DE-SC0020827. Recommended by Associate Editor M. Grover. *(Corresponding author: S. O. Reza Moheimani.)*

The authors are with the Erik Jonsson School of Engineering and Computer Science, The University of Texas at Dallas, Richardson, TX 75080 USA (e-mail: richa.m@utdallas.edu; reza.moheimani@utdallas.edu).

Digital Object Identifier 10.1109/TCST.2024.3363370

B. Existing Methods for Estimation of Surface Parameters

Several methods have been proposed to determine surface electronic properties. These techniques are generally referred to as scanning tunneling spectroscopy (STS) [8], [17], [18], [19].

When studying the electronic structure of a surface, an important objective is to determine the density of states for a specific location [20]. To do this, the feedback loop is disabled, and the tip is held stationary over the surface; then, the current $I(V)$ is measured as a function of the bias voltage, while the voltage is ramped in both directions. Subsequently, the voltage is returned to the value corresponding to the constant-current imaging mode, and the feedback loop is enabled. The slope of the resulting I–V curve, or dI/dV, provides information on the local density of states (LDOS). Although this conventional spectroscopy method can be effective, it can also be time-consuming. Obtaining I–V spectra for every pixel can take several hours, and the resulting images are often degraded by lateral drift.

The spectroscopic mapping of a surface can be obtained quickly by utilizing a feedback loop and adding a modulation signal to the dc bias voltage at a constant tunneling current. This technique allows for the acquisition of a dI/dV image simultaneously with the topography image for a given dc bias voltage. However, as noted in [21], this method has two main drawbacks. First, the resulting images are likely to be noisy due to the small amplitude of the modulation voltage. Increasing the amplitude of the modulation voltage to obtain a better signal-to-noise ratio may disrupt the feedback loop, resulting in the degradation of the topography image. Second, the $I(V)$ information at very low voltages cannot be accurately captured since the tip–sample distance keeps changing, and the tip may collide with the surface for small sample bias voltages ranging from 0.1 to 1 V.

To address these issues, we proposed the use of notch filters tuned to the harmonics of the fundamental modulation frequency, while STM is operating in the spectroscopy mode [21]. Thus, current components at multiples of the modulation frequency are rejected, enabling the feedback loop to operate undisturbed even as the amplitude of the modulation voltage increases. This results in images with a higher signal-to-noise ratio.

Another issue with conventional spectroscopy is that the tip–sample distance constantly changes, making it challenging to capture $I(V)$ information at very small voltages. We addressed this issue in a separate study [22] by closing the feedback loop on the natural logarithm of differential conductance, $\ln(dI/dV)$, instead of the natural logarithm of tunneling current. In this approach, the tip–sample distance is regulated even when the applied sample dc bias voltage is zero, allowing for information about the engagement of electronic states for the full range of sample bias voltage. The I–V curve can be obtained orders of magnitude faster than the conventional spectroscopy method.

While these spectroscopic methods provide valuable information on the electronic structure of a surface, they have limitations in directly measuring the surface conductivity, σ. The methods discussed in [21] and [22] are significantly faster than the methods discussed in [8], [17], [18], and [19]. However, all these methods obtain the differential conductance, dI/dV, which is considered as an approximate representation of the surface conductivity, σ, since surface variations, h, affect the dI/dV measurements obtained from a lock-in amplifier (LIA). In addition, these methods do not provide a direct means of distinguishing between the effects of electronic and physical properties of the surface on the controller output.

C. Contributions of This Article

The contributions of this article are twofold. First, we introduce a novel method for directly estimating surface conductivity, σ, from experimental measurements obtained during constant-current STM at a specific sample bias voltage. This approach is based on a Kalman filtering estimation technique when process noise is modeled as colored noise as opposed to white noise as in [23]. It turns out that colored process noise modeling is more consistent with the physics of the surface and the data obtained from regular STM imaging. The second novel addition to the preliminary results discussed in [23] is employing a disturbance observer to estimate surface variations that are otherwise difficult to differentiate in the controller output as discussed in Section I-A. To substantiate our observations from estimated surface parameters, we have carried out hydrogen depassivation lithography on a $\mathrm{Si}(100) - 2 \times 1 : \mathrm{H}$ passivated surface, as opposed to the experimental results presented in [23]. To the authors' knowledge, this is the first successful demonstration of how surface electronic properties and topographic features can be decoupled in STM.

In the remainder of this article, we briefly present the system modeling and theoretical background of the work in Section II. The proposed method based on the Kalman filtering estimation technique is illustrated in Section III. We demonstrate the experimental results in Section IV and conclude this article in Section V.

II. Control Structure and the STM Parameters

In this section, we discuss the quantum mechanical phenomena behind the tunneling current and various parameters governing the tunneling current established between the sample and the tip. We also discuss a modification to the feedback control system architecture, the identification of open-loop STM plant dynamics, and the self-tuning proportional–integral (PI) method required for modeling in this work.

A. Tunneling Current and the STM Parameters

When a bias voltage is applied to the sample, electrons tunnel through the vacuum between the electrically grounded sharp tip and the sample due to a quantum mechanical phenomenon known as tunneling. This tunneling current, i, is directly proportional to the sample bias voltage and is highly sensitive to the tip–sample distance. Under normal operating conditions, the relationship between tunneling current and

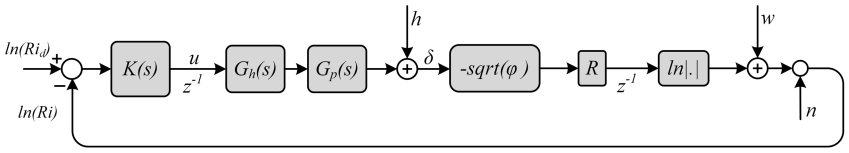

Fig. 2. Block diagram of the STM feedback loop in the constant-current mode. The controller command u is amplified by the high-voltage amplifier G_h, which drives the piezoactuator G_p. As the tip is scanned across the surface, variations in surface topography appear as a disturbance h, causing a change in the tunneling current. This change is regulated by the controller $K(s)$ by adjusting the tip–surface gap, δ. The preamplifier with a gain of R converts the sub-nanoampere range current to a measurable voltage. Here, n is the measurement noise and $w = \ln(R\sigma V_b)$ is constant.

tip–sample gap is approximately exponential [2], [15], [24], that is,

$$i = \sigma V_b e^{-1.025\sqrt{\varphi}\delta} \tag{1}$$

where V_b (in V), σ (in nA/V), δ (in nm), and φ (in eV) are the bias voltage, the local density of states of the sample, tip–sample distance (tip height), and the "work function" or "local barrier height" (LBH), respectively. The quantum tunneling phenomenon transforms the tip–sample separation, δ, into a current, i. This sub-nanoampere range current is converted to a measurable voltage using a preamplifier gain of R. The natural logarithm of the transformed current linearizes the nonlinear exponential dependence of tunneling current on tip–sample distance (1) as

$$ln(Ri) = \ln(R\sigma V_b) - 1.025\sqrt{\varphi}\delta. \tag{2}$$

The tunneling current, i, is a function of several parameters described by (2). Understanding the implications of each parameter on $ln(Ri)$ is vital to the design of the STM control system.

1) ln(Ri) and δ: The linear relationship between the natural logarithm of the tunneling current, (ln(Ri)), and the distance between the STM tip and the sample surface, δ, have important implications on the control of the STM. By utilizing a linear feedback system to maintain a constant tunneling current, the STM can effectively "feel" the shape of the sample surface and produce a high spatial resolution topographic image.

2) ln(Ri) and φ: In addition to providing a high-resolution topographic image of a sample surface, specifically, by measuring the logarithmic derivative of the tunneling current with respect to the tip–sample distance, one can obtain a measure of the work function (φ) of the sample. The LBH or work function is defined as the minimum energy required to remove an electron from a solid surface. It represents the physical and electronic properties of the sample surface

$$\varphi = 0.952\left(\frac{d}{d\delta} ln(Ri)\right)^2. \tag{3}$$

As the STM tip scans across the sample surface, the barrier height can change due to variations in the physical and spatial surface properties. Suppose that the tip encounters an atom on the surface with a different chemical composition or electronic structure than the surrounding atoms. In that case, the barrier height may be higher or lower than the surrounding areas, resulting in variations in the tunneling current. Also, $\sqrt{\varphi}$ contributes to the gain of the STM transfer function that the controller regulates, as shown in Fig. 2. Therefore, this term in the tunneling current equation becomes an essential parameter for the estimation [16], [25], [26]. The accurate barrier height estimation investigated in [16], [25], and [26] is one of the highlights of STM control research.

3) ln(Ri) and σ: In (1), σ, which is known as surface conductivity, depends on the electronic properties of the material and changes from atom to atom on surfaces with defects, adatoms, and buried dopants. Conventionally, to acquire local density of states (LDOS) or differential conductance at a bias voltage, V_b, the I–V curve is obtained by keeping the tip at a fixed position and ramping the voltage in both directions [27]. For a small bias voltage, the first derivative of the total tunneling current is proportional to the LDOS of the sample surface [28]

$$\frac{dI}{dV} \propto \sigma. \tag{4}$$

Since the tip height tends to vary during a scan on surfaces with many defects or buried dopants, dI/dV measurements cannot accurately reflect spatial variations in σ. This parameter contributes to the total tunneling current, and thus, the information it holds needs to be estimated as the tip scans the surface.

B. Closed-Loop STM System Identification

In STM, closed-loop system identification is a crucial step in implementing model-based advanced control techniques. This process involves identifying the transfer function that relates the control signal to the natural logarithm of the resulting tunneling current, and it is performed while the feedback loop is enabled in constant-current mode, as shown in Fig. 3.

The frequency response functions (FRFs) of the system were obtained by adding exogenous inputs, r_e, to the error signal, and r_u to the controller output and then experimentally determining the transfer functions as discussed in [29]. Specifically, four transfer functions were obtained through this process

$$G_{r_eU}(j\omega) = \frac{K(j\omega)}{(1 + K(j\omega)G(j\omega))} \tag{5}$$

$$G_{r_eY}(j\omega) = \frac{K(j\omega)G(j\omega)}{(1 + K(j\omega)G(j\omega))} \tag{6}$$

$$G_{r_uU}(j\omega) = \frac{1}{(1 + K(j\omega)G(j\omega))} \tag{7}$$

$$G_{r_uY}(j\omega) = \frac{G(j\omega)}{(1 + K(j\omega)G(j\omega))}. \tag{8}$$

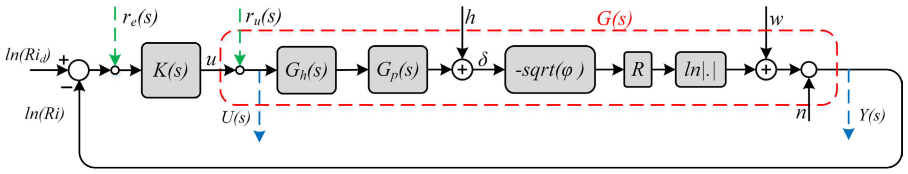

Fig. 3. STM feedback loop for system identification. n, h, $ln(Ri)$, $\ln(R\sigma V_b)$, and y_p represent sensor noise, surface variation, the set point, and log of measured tunneling current, respectively. r_e and r_u are the exogenous sinusoidal signals with varying frequency (in green), and output responses are $U(s)$ and $Y(s)$ (in blue).

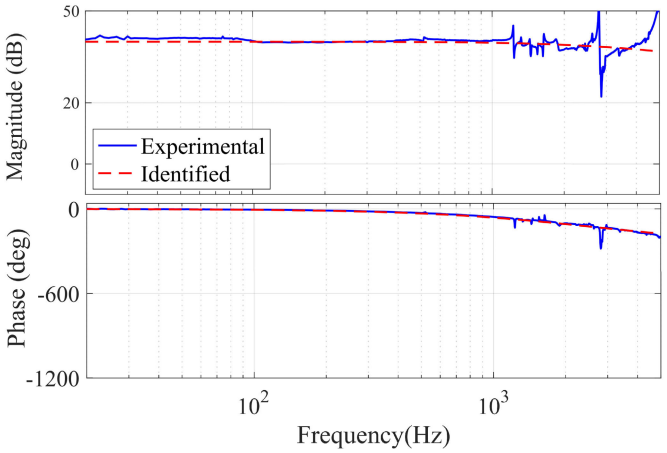

Fig. 4. Frequency response of the STM obtained through closed-loop system identification. The measured FRF and estimated $G(s)$ are shown. Since the STM typically operates in a closed-loop bandwidth of 100 or 200 Hz, the fit model adequately captures the plant dynamics over the frequency range of interest.

The STM transfer function $G(s)$ is obtained by dividing the FRFs at each frequency point

$$G(j\omega) = \frac{G_{r_eY}(j\omega)}{G_{r_eU}(j\omega)} = \frac{G_{r_uY}(j\omega)}{G_{r_uU}(j\omega)}. \tag{9}$$

We can experimentally characterize the STM and identify $G(s)$ while measuring and recording only two signals: the tunneling current $ln(Ri)$ obtained from transimpedance amplifier (sensor) with gain R and the control signal u after digital computation, as the feedback loop is enabled. The FRFs are measured when the tip is engaged and the tunneling current establishes over an atom on the surface. The transfer function $G(s)$ captures piezoactuator dynamics and effects of the current tunneling phenomenon.

To obtain the closed-loop FRF of a home-built STM, we conducted experiments using an ONOSOKKI CF 9400 FFT analyzer. The FRFs were obtained by adding a frequency sweep from 10 to 5000 Hz to the error signal. We divided this frequency sweep range into three intervals with different averaging and input sweep frequency amplitudes to maintain a good signal-to-noise ratio in the low-frequency range and prevent tip oscillation near the resonance frequency.

Once we obtained the STM's FRF using the method proposed in [29], we fit a transfer function, $G(s)$, to obtain a model as

$$G(s) = \frac{-3.27 \times 10^6 s + 4.425 \times 10^{10}}{s^2 + 4.94 \times 10^4 s + 4.467 \times 10^8}. \tag{10}$$

Fig. 4 depicts the frequency response of the STM plant and the Bode diagram of the estimated transfer function. The STM generally operates with a closed-loop bandwidth of 100–200 Hz and the presented model sufficiently captures the low-frequency dynamics of the system that are relevant to our estimation procedure. In [29], it has been established and also observed in Fig. 2 that the dc gain of $G(s)$ is

$$\left\|G(j\omega)\right\|_{\omega=0} = 1.025\sqrt{\varphi}k_h k_p \tag{11}$$

where k_h is the dc gain of the high-voltage amplifier, $G_h(s)$, and is a constant. Also, k_p is the dc gain of the piezoactuator $G_p(s)$, which depends on the material properties and is, therefore, a constant. Thus, any changes in the dc gain of the STM are attributed to the change in the LBH of the surface, i.e., φ.

In [29], we reported variations in the observed dc gain ranging from 48 to 60 dB for the system used in these experiments and a hydrogen-passivated silicon surface. Once the PI controller parameters are fixed, variations in the LBH can lead to system instability, resulting in a tip–sample crash. To address this issue, a self-tuning adaptive method was implemented in [29] to estimate changes in the LBH in real time and compensate for these changes by adjusting the PI gain. This method is discussed briefly in Section II-C as it is vital for developing the estimation methodology in this article.

C. Self-Tuning Z-Axis Control System

We consider the simplified current model (1), which leads to the STM control loop shown in Fig. 5 with a self-tuning PI controller to compensate for LBH variations in [30]. For LBH estimation, we add a high-frequency sinusoidal signal $r(j\omega)$ to the error signal as shown in Fig. 5 and then record the responses at the output of the controller and the output of the preamplifier, $Y(s)$ and $U(s)$, respectively. The frequency of the modulating signal should be above the closed-loop bandwidth of the system since the topography information lies in the low-frequency region. Also, it should be carefully selected so that it avoids exciting the system's resonance frequencies. The above procedure can be stated as

$$Y(j\omega) = \frac{K(j\omega)G(j\omega)}{1 + K(j\omega)G(j\omega)} r(j\omega) \tag{12}$$

$$U(j\omega) = \frac{K(j\omega)}{1 + K(j\omega)G(j\omega)} r(j\omega). \tag{13}$$

We are interested in the ω component of Y and U in the given control arrangement. Therefore, the responses are passed through the bandpass filter tuned at the ω frequency. The width

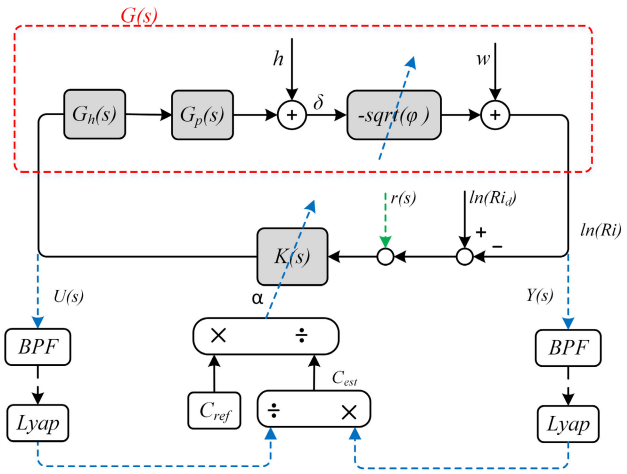

Fig. 5. Z-axis control system block diagram with a self-tuning PI controller.

of the passband determines the LBH estimation bandwidth. Then, these filtered signals are passed through a Lyapunov filter [31] to estimate the magnitudes of the responses. Dividing (12) by (13) yields $G(j\omega)$, i.e.,

$$\frac{Y(j\omega)}{U(j\omega)} = G(j\omega). \tag{14}$$

The magnitude of $G(j\omega)$ is proportional to LBH

$$\frac{\|Y(j\omega)\|}{\|U(j\omega)\|} = \|G(j\omega)\| \propto \|G(0)\| \propto \sqrt{\varphi}. \tag{15}$$

This study [25] demonstrates that the work function of a $\mathrm{Si}(100)-2\times 1:\mathrm{H}$ passivated surface changes as the tip moves from a hydrogen (H) atom to a silicon (Si) atom, which in turn affects the LBH. These changes in LBH affect the loop gain of the STM control loop, which can cause instability in the system.

To address this issue, the simplified model depicted in Fig. 5 shows that as the dc gain of the system, represented by $G(s)$, changes due to the variable nature of LBH (shown in blue arrow), the PI gain adapts (shown in blue arrow) accordingly to prevent the tip from crashing into the surface. The closed-loop system gain is kept constant by multiplying the PI controller with α (LBH gain norm), which is tuned to account for changes in LBH estimations. This makes the STM Z-axis control self-tunable, ensuring stable and accurate measurements. In Fig. 5

$$\alpha = \frac{C_{\text{ref}}}{C_{\text{est}}}. \tag{16}$$

Also, the PI controller is defined as

$$K(s) = k_i\left(\frac{1}{s} + \frac{1}{\omega_c}\right) \tag{17}$$

where k_i is the overall gain and ω_c is the corner frequency.

The STM control loop depicted in Fig. 5 relies on the accurate determination of C_{ref}, which is obtained by modulating the set point and recording the output signal $d(lnI)/(dz)$ using an LIA before the scanning process begins. The result of this approach is shown in Fig. 6, where we observe LBH varying from high to low over a 48 × 48 nm area of a $\mathrm{Si}(100)-2\times 1:\mathrm{H}$ passivated surface. In this type of surface, the lithography area appears as a bright contrast, but in the LBH image, the contrast is dark as the LBH is lower over dangling bonds (missing H-atoms).

This variability in LBH challenges the stability of the control loop, but the self-tuning PI controller implemented in this system adjusts α to make the overall closed-loop gain constant despite changes in LBH. This ensures that the scanning process remains stable and accurate.

III. Estimation of Surface Variations and Conductivity

In this section, we set up an augmented Kalman filter (KF) to estimate surface conductivity, σ, which appears as an output disturbance, $\ln(R\sigma V_b)$, in Fig. 7. We will then integrate the estimated output disturbance into a disturbance observer to estimate surface height variations, h, which appear as an input disturbance.

A. STM Modeling for Estimation

In the STM control system, depicted in Fig. 2, the natural logarithm of the tunneling current is compared to the logarithm of the reference current and the resulting error signal is fed into a PI controller. The output of the controller drives the Z-axis piezoactuator $G_p(s)$ via a high-voltage amplifier, $G_h(s)$, thereby maintaining a constant current by adjusting the tip height. Here, h denotes the atomic surface height, i.e., the actual surface topography. Scan speed is typically selected so that most surface features fit within the closed-loop bandwidth. Thus, h can be projected as the input disturbance, h_i to the plant, shown in Fig. 7. Note that $G(s)$ is the combined dynamics of all STM components in Fig. 2.

In STM, the control signal, u, is plotted as the topography signal. However, it is clear from Fig. 2, and its simplified version in Fig. 7, that the control signal encompasses changes in the topography features, h, as well as electronic and chemical properties of the surface (such as variations in σ and φ). Furthermore, $w = \ln(R\sigma V_b)$ is a component of the tunneling current that arises from the electronic properties due to the tip–sample interaction. Hence, w can be modeled as the output disturbance to the states of the STM plant. Previous studies [26] have assumed that $\ln(R\sigma V_b)$ is constant, as depicted in Fig. 2.

System identification experiments are performed, while the tip is stationary with respect to the surface. This means that the model does not capture the effect of LBH variations that appear as a variable gain as the tip scans across the surface [30]. The change in LBH is compensated by tuning the PI gain in real time, based on LBH estimation discussed in [25] and summarized above. Thus, the loop gain becomes constant validating the LTI model of the STM as

$$\begin{aligned} \dot{x}_p &= Ax_p + B_u u + B_u h_c \\ y &= C_p x_p + w + n. \end{aligned} \tag{18}$$

The STM model, denoted as $G(s)$ in (10), is characterized by state variables, $x_p \in \mathbb{R}^{(2\times 1)}$, a state transition matrix, $A \in \mathbb{R}^{(2\times 2)}$, a control input matrix, $B_u \in \mathbb{R}^{(2\times 1)}$, and a

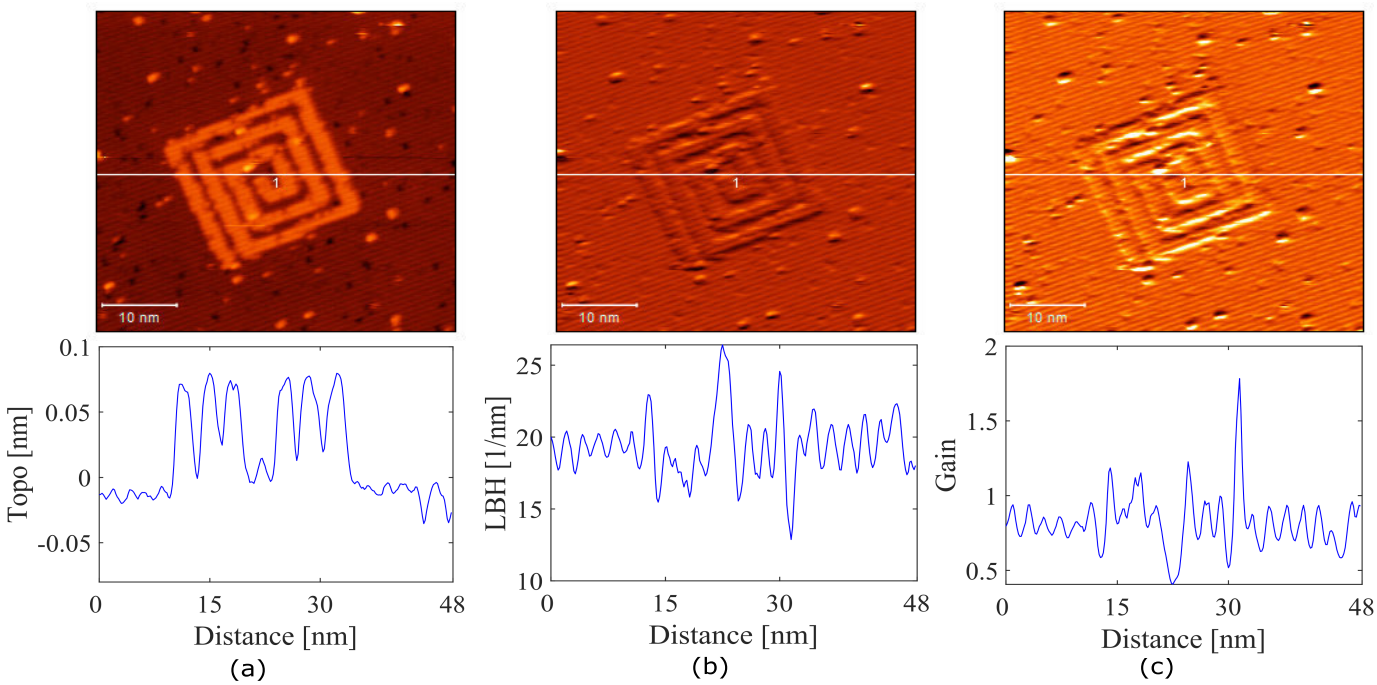

Fig. 6. Top and bottom rows, respectively, show the LBH image and the cross-sectional profile (over a horizontal line in the middle of the image) of a Si(100) $-$ 2 $\times$ 1 : H passivated surface. (a) Detrended topography. (b) LBH, i.e., C_{est}. (c) LBH gain norm, α. Spiral lithography has been performed on Si(100) $-$ 2 $\times$ 1 : H passivated surface to show variations in LBH as the tip moves from H-atom to Si atom.

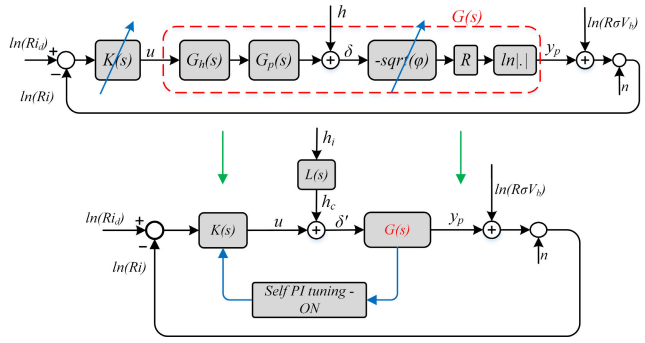

Fig. 7. STM's modified Z-axis control loop for Kalman Filtering modeling. Here, n, h_c, ln(Ri), ln($R\sigma V_b$), and y_p represent sensor noise, projected surface variation modeled as an input disturbance, the logarithm of tunneling current, natural log of conductivity modeled as an output disturbance, and output of the STM plant, respectively. $L(s)$ is the shaping filter. In this scheme, the LBH estimation and the self-tuning PI gain adaptation method run in the background.

measurement matrix, $C_p \in \mathbb{R}^{(1\times 2)}$. The control input, u, and sensor output, y, which represents the tunneling current, are associated with the STM control. As illustrated in Fig. 7, the output of the STM plant is represented by y_p. However, it is inaccessible and cannot be measured directly.

B. Estimation of $ln(R\sigma V_b)$

The KF is a powerful tool for estimating the state of linear stochastic dynamic systems based on observations, a mathematical model of the system, and statistical information about the process and measurement noise [32]. Successful implementation of a KF requires access to a good model of the process, which could be obtained through system identification experiments. Kalman filtering has been applied to other types of scanning probe microscopes in the past [33], [34].

In sequential KF estimation, the estimated states and their associated uncertainties are propagated over time using an error covariance matrix [32], [35], [36]. This covariance propagation is used to monitor the convergence of the estimation. Assume that a Gaussian noise process simplifies the posterior estimation of states and results in an optimal estimator, making it a valuable tool in various applications as discussed in [32], [35], and [36].

Here, we discretize the STM model in (18) as

$$\begin{aligned} x_k &= A_{k-1}x_{k-1} + B_{u_{k-1}}u_{k-1} + B_{u_{k-1}}h_{c_{k-1}} \\ y_k &= C_k x_{k-1} + w_k + n_k \end{aligned} \tag{19}$$

where $h_{c_k} \sim \mathcal{N}(0, Q_{h_c})$ and $n_k \sim \mathcal{N}(0, \tilde{R})$ denote process and measurement noise with covariance matrix $Q_{h_c} \in \mathbb{R}$ and $\tilde{R} \in \mathbb{R}$, respectively. Here, the process noise, h_{c_k}, is modeled as filtered white noise to capture the effects of surface height variations, h, such that the filtered noise remains Gaussian [37]. The shaping filter $L(s)$, in Fig. 7, is a low-pass filter (LPF) that considers the periodicity of dimer rows on the surface. This approach provides a more accurate representation of the actual noise while preserving the observability of the augmented system.

It is worth noting that the power spectrum of the controller output exhibits significant energy in the low-frequency region, indicating the importance of modeling the noise as colored rather than white.

The state-space model of LPF when discretized using the Tustin method is

$$\begin{aligned} x_{f_{k+1}} &= A_{f_k}x_{k-1} + B_{f_k}h_{i_k} \\ h_{c_k} &= C_{f_k}x_k + D_f h_{i_k}. \end{aligned} \tag{20}$$

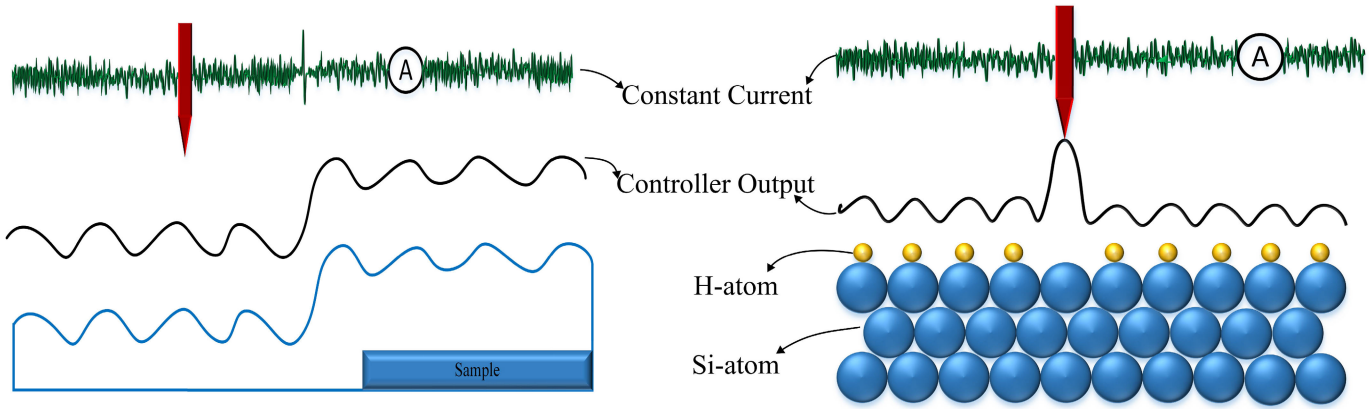

Fig. 8. (a) Expected controller output as the tip scans the surface in STM. (b) Actual controller output due to electronic/physical properties of the surface in constant-current mode.

To estimate the unknown disturbance, w, the state augmentation technique is used [23], [32], [35], [36]. The unknown disturbance w is regarded as a state variable and augmented to the state vector as follows:

$$X_k = \begin{bmatrix} x_k \\ w_k \\ x_{f_k} \end{bmatrix}.$$

The unknown disturbance w is modeled as a constant affected by a small artificial noise h_w as

$$w_{k+1} = w_k + h_{w_k}, \quad \text{where} \quad h_{w_k} \sim \mathcal{N}(0, Q_w). \tag{21}$$

The state augmentation process transforms a disturbance estimation problem into a standard discrete-time KF. The augmented state equation is driven by the process noise h_{i_k} and h_{w_k}. The augmented state-space model for the Kalman filtering technique is shown as follows:

$$\begin{bmatrix} x_{k+1} \\ w_{k+1} \\ x_{f_{k+1}} \end{bmatrix} = \underbrace{\begin{bmatrix} A_k & 0 & B_k C_{f_k} \\ 0 & 1 & 0 \\ 0 & 0 & A_{f_k} \end{bmatrix}}_{A_{\text{aug}}} \begin{bmatrix} x_k \\ w_k \\ x_{f_k} \end{bmatrix} + \underbrace{\begin{bmatrix} B_{u_k} \\ 0 \\ 0 \end{bmatrix}}_{B_{\text{aug}}} u_k$$
$$+ \underbrace{\begin{bmatrix} B_{u_k} D_{f_k} & 0 \\ 0 & 1 \\ B_{f_k} & 0 \end{bmatrix}}_{G_{\text{aug}}} \begin{bmatrix} h_{i_k} \\ h_{w_k} \end{bmatrix}$$
$$Y_k = \underbrace{\begin{bmatrix} C_k & 1 & 0. \end{bmatrix}}_{C_{\text{aug}}} \begin{bmatrix} x_k \\ w_k \\ x_{f_k} \end{bmatrix} + n_k.$$

With this augmented state vector, x_k and w_k are estimated simultaneously using the KF algorithm, given that $(A_{\text{aug}}, C_{\text{aug}})$ is observable and $(A_{\text{aug}}, G_{\text{aug}})$ is controllable.

The prediction–correction steps in the KF algorithm can be applied as follows.

1) *Prediction Step:*

a) A priori error covariance prediction

$$P_k^- = A_{\text{aug}_{k-1}} P_{k-1}^+ A_{\text{aug}_{k-1}}^T + G_{\text{aug}_{k-1}} Q_{k-1} G_{\text{aug}_{k-1}}^T. \tag{22}$$

b) A priori state prediction

$$\hat{X}_k^- = A_{\text{aug}_{k-1}} \hat{X}_{k-1}^+ + B_{\text{aug}_{k-1}} u_k. \tag{23}$$

2) *Correction Step:*

a) Kalman gain calculation

$$K_k = P_k^- C_{\text{aug}_k}^T \left(C_{\text{aug}_k} P_k^- C_{\text{aug}_k}^T + R_k \right)^{-1}. \tag{24}$$

b) A posteriori error covariance calculation

$$P_k^+ = P_k^- - K_k C_{\text{aug}_k} P_k^-. \tag{25}$$

c) A posteriori state calculation

$$\hat{X}_k^+ = \hat{X}_k^- + K_k \left(Y_k - C_{\text{aug}_k} \hat{X}_k^- \right). \tag{26}$$

The subscript k is the sequence of time, and $\hat{X}$ is an estimate of both the states in X.

C. Estimation of Surface Height Variations, h

In Section II, we pointed out that the tunneling current, i, is influenced by three surface parameters: LBH, surface conductivity, σ, and surface features, h. A feedback controller adjusts the distance between the tip and the sample to maintain a constant current, as shown in Fig. 8(a). The controller output, u, is then used to represent the surface topography. However, this assumption is only correct as long as surface electronic properties, captured by the output disturbance, w, in Fig. 7, remain unchanged as the tip scans across the surface. Otherwise, as illustrated in Fig. 8(b), the controller output may not exactly map the surface features. Despite this, information about the true surface topography does exist in the control signal, providing an opportunity to estimate the actual surface height variations from the overall system dynamics and the measured current.

To estimate the surface variations, h, we design a disturbance observer [38], as depicted in Fig. 9. The estimated STM plant model is denoted as G_n, and an LPF is applied with a transfer function of Q. The input and output disturbances to the plant are represented by h_c and $\ln(R\sigma V_b)$, respectively. The estimate of the output disturbance is denoted as $\ln(R\sigma V_b)_{\text{est}}$.

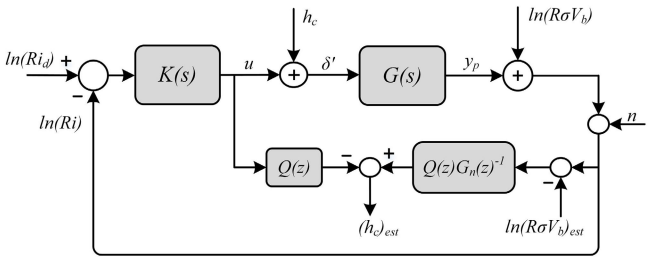

Fig. 9. Disturbance observer for estimating the surface variations, h, modeled as h_c.

The output of the plant can be expressed as follows:

$$y = G_n(u + h_c) + \ln(R\sigma V_b)_{\text{est}}. \tag{27}$$

Equation (27) is reordered to estimate the surface variation $h_{c_{\text{est}}}$ entering the STM

$$h_{c_{\text{est}}} = G_n^{-1}(y - \ln(R\sigma V_b)_{\text{est}}) - u. \tag{28}$$

The accuracy of the estimation of surface variation depends on the accurate estimation of $\ln(R\sigma V_b)$. Obtaining a good estimate of surface conductivity, σ, relies on the modeling of process noise. Therefore, in this article, we have modeled process noise as colored noise, as opposed to results presented in [23] based on the process noise modeled as white noise.

1) Working Principle of Disturbance Observer: Before implementing the disturbance observer, it is necessary to find the inverse of the estimated STM plant. However, this can be challenging due to the nonminimum phase (NMP) zeros of the plant. Several techniques have been proposed to deal with this issue [39]. We use the zero-magnitude error tracking controller (ZMETC) since it achieves unity gain at all frequencies. This method amplifies high-frequency components. Hence, there is a need to include an LPF, with unity gain at low frequencies, to obtain the inverse of the plant.

The estimated plant model $G_n(z)$ is represented by $A(z)$, which includes poles, and $B_s(z)$ and $B_u(z)$, which include stable and unstable zeros of the system, respectively, that is,

$$G_n(z) = \frac{B(z)}{A(z)} = \frac{B_s(z)B_u(z)}{A(z)}. \tag{29}$$

The unstable zeros $B_u(z)$ are expressed as an nth-order polynomial

$$B_u(z) = b_{u_n}z^n + b_{u_{n-1}}z^{n-1} + \ldots + b_{u_0} \tag{30}$$

where n is the number of NMP zeros. According to ZMETC, the approximate inverse of $G(z)$ can be obtained by reflecting unstable zeros to stable poles with respect to the unit circle, i.e., $z_{u_i} \to 1/z_{u_i}$. Therefore, $\tilde{G}_n(z)^{-1}$ can be obtained as

$$\tilde{G}_n(z)^{-1} = \frac{A(z)}{B_s(z)B_u^*(z)} \tag{31}$$

where

$$B_u^*(z) = b_{u_0}z^n + b_{u_1}z^{n-1} + \ldots + b_{u_n}. \tag{32}$$

In this disturbance observer, to suppress high-frequency noise in measurements, an LPF is needed to fine-tune the open loop for estimating the surface variations, h, as depicted in Fig. 9. We select this LPF to be identical to ZMETC's $Q(s)$. Typically, $Q(s)$ is designed as $1/(\omega_l s + 1)$, where ω_l is a tuning parameter that determines the level of disturbance filtering. The cutoff frequency of the LPF, $Q(s)$, is $\omega_l = 300$Hz. The cutoff frequency was selected to reject undesirable high-frequency noise. As the available information suggests that disturbances and surface variations, h, only exist in the low-frequency range, a 4th-order LPF with unity dc gain is implemented as $Q(s)$. Also, the 4th-order LPF was selected to minimize the phase lag introduced by the filter on the estimation. $Q(s)$ is fine-tuned around the above values iteratively to meet the desired performance. This LPF is then discretized at 100 kHz.

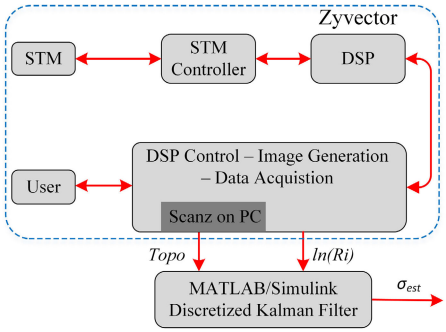

Fig. 10. Schematics of the experimental setup including STM, Zyvex Labs' user interface Scanz and Zyvector control box. Also shown is the implementation of a discretized KF in MATLAB/Simulink using the experimentally obtained data to estimate surface conductivity σ.

IV. Experimental Results

In this section, we present the experimental results obtained by imaging a $\text{Si}(100) - 2 \times 1 : \text{H}$ passivated surface with an ultrahigh vacuum (UHV) STM and apply our approach to estimate the surface conductivity, σ, and surface height variations, h.

A. Experimental Setup

The experiments were performed on a $\text{Si}(100) - 2 \times 1 : \text{H}$ passivated surface with a tungsten tip. The scanner is operated in UHV at 10^{-11} torr and at room temperature. A Femto DLPCA-200, low-noise current preamplifier with a gain of 10^9 and bandwidth of 1 kHz, measures the tunneling current. The preamplifier output is sent back to the STM controller for signal conditioning and then to the digital signal processing (DSP) for digitization. Finally, the signal is returned to the computer for image processing, as shown in Fig. 10. The STM controller is implemented in a 20-bit DSP unit TMS320C6713 running at 100 kHz. This sampling frequency is used for recording signals and generating the image. The Scanz[1] software unit provides a graphical user interface to set the scan parameters, controller gains, and mode of operation of STM [40]. The two experiments were conducted in the imaging mode on a different $\text{Si}(100) - 2 \times 1 : \text{H}$ passivated surface at a sample bias voltage of -2.5 V with tunneling current set points of 0.75 and 0.5 nA.

[1]Trademarked.

TABLE I
PARAMETERS FOR EXPERIMENTAL SETUP

Parameter	Value
Bias Voltage, V_b	-2.5 V
Current set-point, i	0.75/0.5 nA
Rastering speed	100 nm/s
Modulation frequency	2 kHz
Sampling frequency	100 kHz
LBH estimation Bandwidth	400 Hz
Gain of G_h	13.5
Piezo Material sensitivity of G_p	54 nm/V
LPF, $Q(s)$ corner frequency, ω_l	$2 \times pi \times 300$ rad/sec

B. Results

A 24 $\times$24 nm area of a Si(100) $-$ 2 $\times$ 1 : H passivated surface is imaged at a resolution of 16 000 $\times$ 128 pixels. The LBH estimation algorithm [25] and the self-tuning PI controller method are implemented in Scanz. Table I shows the main parameters used for imaging, LBH estimation, and controller tuning in this experiment. The modulation frequency selected for LBH estimation is 2 kHz, significantly larger than the closed-loop system bandwidth. A topography image obtained by Scanz and Zyvector[1] from a Si(100) $-$ 2 $\times$ 1 : H passivated surface is shown in Fig. 11(a) and (b). The image is a plane surface with dimers of hydrogen atoms (appearing as orange-colored rows), bright spots (dangling bonds, i.e., missing H-atoms), and dark spots (missing dimer rows). The surface also includes irregular, brighter spots. The nature of these spots is not clearly known, but they represent contamination. Two separate experiments were conducted several days apart on two different samples, with different tips and different tunneling currents to implement our approach on different surface image data. Lithography was performed to understand the estimation of surface conductivity, σ, and surface variations, h, better. The obtained images have a tilt (trend) moving downward as the tip scans the surface line by line. The tilt in the surface can be in both directions depending on the relative orientation of the surface of Si(100) $-$ 2 $\times$ 1 : H with respect to the tip.

Surface height variations, h, affect the tunneling current, causing it to deviate from the set point. A PI controller maintains a constant natural log of tunneling current by adjusting the tip–sample separation, δ. Consequently, the controller output, u, reflects the topography of the surface, including any step edges or tilts. A KF estimator is designed to account for stationary process noise caused by such variations. The STM image obtained from Scanz is postprocessed in MATLAB to remove the trend in the topography image data, resulting in detrended topography data in displacement units (in nm). These data are converted from control voltage using a calibration factor of 540 nm/10 V, with 128 scan lines containing 16 000 measurements obtained at sampling intervals of 10 μs. The detrended topography data, along with the natural logarithm of tunneling current, are fed as inputs to the discretized KF model, which is implemented in MATLAB/Simulink at a sampling frequency of 100 kHz. To set the measurement noise covariance, denoted by $\tilde{R}$, the variance ($\sigma^2_{\tilde{R}}$) of the signal ln(Ri) is used. This signal is recorded using a dSPACE system and imported into MATLAB to obtain the variance of measurement noise, with $\tilde{R}$ chosen as $\tilde{R}_1 = 0.04$ and $\tilde{R}_2 = 0.12$, respectively, for the first and second experiments. The process noise covariance matrix, Q, is the only tunable variable determining the estimation bandwidth. To avoid noisy state estimations, Q is selected as large as possible while still maintaining stability, with $Q_1 = \text{diag}(10^{-5}, 10^{-6})$ and $Q_2 = \text{diag}(10^{-5}, 10^{-5})$. The discretized KF is then run sequentially in MATLAB to obtain an estimate of $\ln(R\sigma V_b)$ for every scan line. With the preamplifier gain, R, and the sample bias voltage, V_b known, the estimate of surface conductivity, σ, can be determined.

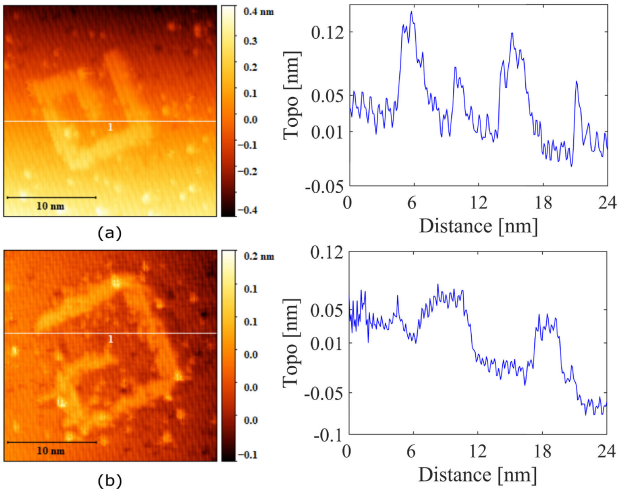

Fig. 11. Topography images of two different Si(100) $-$ 2 $\times$ 1 : H passivated surface as obtained from Scanz and Zyvector control before image processing. Before imaging, spiral patterns of Si dangling bonds were generated by desorbing hydrogen atoms from the surface. Sample bias voltage of $-$2.5 V with a tunneling current set point of (a) 0.75 and (b) 0.5 nA. Profile line 1, drawn over both the topography images, is represented in the images on the right side.

The detrended topography, tunneling current, LBH, estimated surface conductivity, and surface variations (true topography) are shown in Fig. 12(a)–(j) with their respective profiles. Profile 1 is superimposed on the spiral lithography and appears as a bright contrast in the first experiment, as shown in Fig. 12(a), with the corresponding change in the profile depicted as three peaks as it is drawn over three lines of lithography. The tunneling current remains constant, as expected, as shown in Fig. 12(b).

To confirm the accuracy of the surface conductivity, σ, estimation, an LBH image is also obtained. As described in Section II, the LBH represents the minimum energy required to remove an electron from the surface. From the image in Fig. 12(c), we observe that the LBH is low over the missing H-atoms (dangling bonds), resulting in the lithography pattern appearing as a dark region. As anticipated, the surface conductivity at this point is high since Si-atoms are more reactive than H-atoms, as evident from the profile of the estimated conductivity in Fig. 12(d). Once we have obtained an estimate of $\ln(R\sigma V_b)$, we utilize this estimation in a disturbance observer as in (28) to estimate the surface height variations, h. Fig. 12(e) shows that the estimation of surface variation results in a dark contrast wherever an H-atom has been removed. The topography profile exhibits troughs over the lithography area. A noticeable difference is observed when

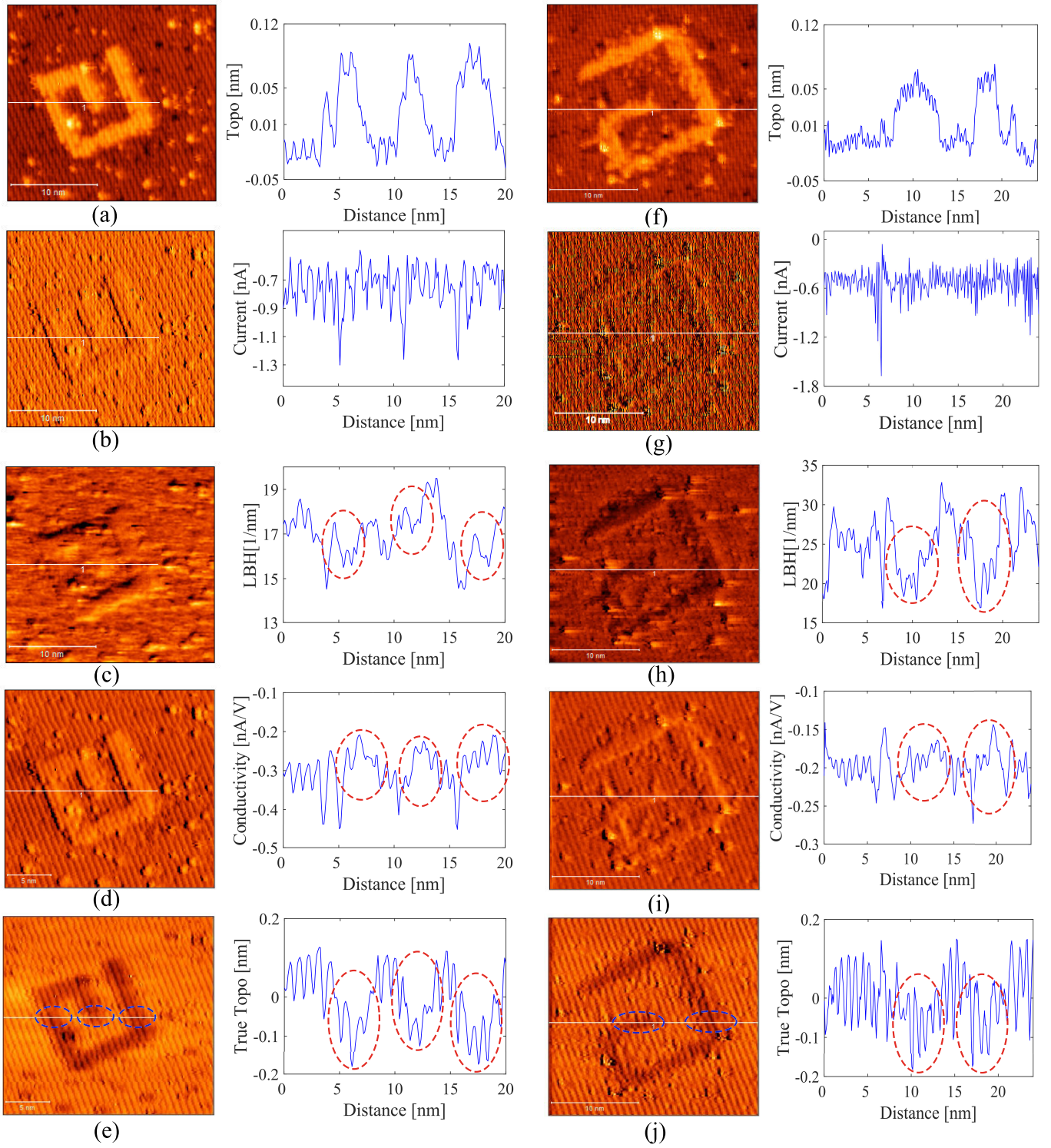

Fig. 12. Images and profiles of lithography in a $Si(100) - 2 \times 1 : H$ passivated surface. (a) and (f) Detrended topography, (b) and (g) tunneling current, (c) and (h) LBH, (d) and (i) estimated conductivity, and (e) and (j) estimated surface variations (true topography). Surface features to observe are circled in (e) and (j) (in blue), and respective surface features are circled in profile (in red).

we compare the topography and surface variation images. While the topography image displays the effects of surface conductivity and surface variations, the surface variation image clearly highlights the true surface topography.

The surface image obtained from the second experiment is plotted in Fig. 11(b). The surface profile over line 1 is sketched next to the topography image. The data obtained in this experiment were significantly noisier than the first experiment, as shown in Fig. 11(a). We followed the same procedure we applied to the first set of experimental data. The effect of higher noise levels is captured by the measurement noise in (19). We again observe that LBH is low on a dangling bond

[see Fig. 12(h)] and that the estimated surface conductivity, σ, is high on dangling bonds [see Fig. 12(i)]. These observations are in agreement with those made based on the first experiment data. The surface variation, h, estimation clearly shows the missing H-atom as a drop in surface height of approximately 100 pm (inside red circle), which is the diameter of the hydrogen atom [see Fig. 12(e) and (j)].

V. Conclusion

In conclusion, we presented a novel framework for estimating surface conductivity, σ, and surface height variations, h, in STM. Our approach uses a KF estimation technique followed by a disturbance observer to decouple the effects of surface variations from surface conductivity. By doing so, we can obtain a more accurate estimation of the true topography map of the surface, overcoming the limitations of conventional STM where the controller output is affected by surface variations and electronic properties. This is the first successful demonstration of decoupling surface variations and electronic properties in STM, making our approach a significant contribution to the field. Our offline estimation method is beneficial when several tips operate in parallel and a large dataset is available for estimation. In [41] and [42], we reported our efforts to fabricate active STM tips based on MEMS technology. In the future, we aim to enable the parallel operation of these MEMS-based STM tips. Compared to conventional methods, which will require a dedicated LIA per tip to obtain surface parameters, we can estimate surface parameters without additional hardware based on this estimation method. Overall, our framework provides a valuable tool for understanding surface properties and their effects on STM imaging.

Acknowledgment

The authors wish to thank James Owen and Nastaran Nikooienejad for fruitful discussions and Zyvex Labs LLC for enabling data collection in this research.

References

[1] G. Binnig, H. Rohrer, C. Gerber, and E. Weibel, "Tunneling through a controllable vacuum gap," *Appl. Phys. Lett.*, vol. 40, no. 2, pp. 178–180, Jan. 1982.

[2] G. Binnig and H. Rohrer, "Scanning tunneling microscopy," *IBM J. Res. Develop.*, vol. 44, nos. 1–2, pp. 279–293, Jan. 2000.

[3] G. Binnig, H. Rohrer, C. Gerber, and E. Weibel, "7×7 reconstruction on Si(111) resolved in real space," *Phys. Rev. Lett.*, vol. 50, no. 2, pp. 120–123, Jan. 1983.

[4] J. H. G. Owen, D. R. Bowler, C. M. Goringe, K. Miki, and G. A. D. Briggs, "Identification of the Si(001) missing dimer defect structure by low bias voltage STM and LDA modelling," *Surf. Sci.*, vol. 341, no. 3, pp. L1042–L1047, Nov. 1995.

[5] J. B. Ballard et al., "Multimode hydrogen depassivation lithography: A method for optimizing atomically precise write times," *J. Vac. Sci. Technol. B, Microelectron., Nanotechnol. Microelectron., Mater., Process., Meas., Phenomena*, vol. 31, no. 6, Nov. 2013, Art. no. 06FC01.

[6] J. W. Lyding, T.-C. Shen, J. S. Hubacek, J. R. Tucker, and G. C. Abeln, "Nanoscale patterning and oxidation of H-passivated Si(100)-2×1 surfaces with an ultrahigh vacuum scanning tunneling microscope," *Appl. Phys. Lett.*, vol. 64, no. 15, pp. 2010–2012, Apr. 1994.

[7] R. A. Wolkow, "Direct observation of an increase in buckled dimers on Si(001) at low temperature," *Phys. Rev. Lett.*, vol. 68, no. 17, pp. 2636–2639, Apr. 1992.

[8] R. M. Feenstra, "Scanning tunneling spectroscopy," *Surf. Sci.*, vol. 299, pp. 965–979, Jul. 1994.

[9] J. W. Lyding, S. Skala, J. S. Hubacek, R. Brockenbrough, and G. Gammie, "Variable-temperature scanning tunneling microscope," *Rev. Sci. Instrum.*, vol. 59, no. 9, pp. 1897–1902, Sep. 1988.

[10] J. A. Stroscio, R. M. Feenstra, and A. P. Fein, "Electronic structure of the Si(111)2×1 surface by scanning-tunneling microscopy," *Phys. Rev. Lett.*, vol. 57, no. 20, pp. 2579–2582, Nov. 1986.

[11] A. I. Oliva, E. Anguiano, N. Denisenko, M. Aguilar, and J. L. Peña, "Analysis of scanning tunneling microscopy feedback system," *Rev. Sci. Instrum.*, vol. 66, no. 5, pp. 3196–3203, May 1995.

[12] I. Ahmad, A. Voda, G. Besançon, and G. Buche, "Robust digital control approach for high performance tunneling current measurement system," *Control Eng. Pract.*, vol. 20, no. 7, pp. 643–653, Jul. 2012.

[13] Y. Sugawara, T. Ishizaka, and S. Morita, "Simultaneous imaging of a graphite surface with atomic force/scanning tunneling microscope (AFM/STM)," *Jpn. J. Appl. Phys.*, vol. 29, no. 8R, p. 1539, Aug. 1990.

[14] A. I. Oliva, M. Aguilar, J. L. Peña, and E. Anguiano, "Experimental determination of the parameters of the feedback system of a scanning tunnelling microscope," *Meas. Sci. Technol.*, vol. 8, no. 5, pp. 501–507, May 1997.

[15] I. Ahmad, A. Voda, and G. Besancon, "Controller design for a closed-loop scanning tunneling microscope," in *Proc. IEEE Int. Conf. Autom. Sci. Eng.*, Aug. 2008, pp. 971–976.

[16] N. D. Lang, "Apparent barrier height in scanning tunneling microscopy," *Phys. Rev. B, Condens. Matter*, vol. 37, no. 17, pp. 10395–10398, Jun. 1988.

[17] R. Hamers, "Atomic-resolution surface spectroscopy with the scanning tunneling microscope," *Annu. Rev. Phys. Chem.*, vol. 40, no. 1, pp. 531–559, Jan. 1989.

[18] B. S. Swartzentruber, A. P. Smith, and H. Jónsson, "Experimental and theoretical study of the rotation of Si ad-dimers on the Si(100) surface," *Phys. Rev. Lett.*, vol. 77, no. 12, pp. 2518–2521, Sep. 1996.

[19] R. J. Hamers and D. G. Cahill, "Ultrafast time resolution in scanned probe microscopies: Surface photovoltage on Si(111)–(7×7)," *J. Vac. Sci. Technol. B, Microelectron. Nanometer Struct. Process., Meas., Phenomena*, vol. 9, no. 2, pp. 514–518, Mar. 1991.

[20] R. M. Feenstra, J. A. Stroscio, J. Tersoff, and A. P. Fein, "Atom-selective imaging of the GaAs(110) surface," *Phys. Rev. Lett.*, vol. 58, no. 12, pp. 1192–1195, Mar. 1987.

[21] H. Alemansour, S. O. R. Moheimani, J. H. G. Owen, J. N. Randall, and E. Fuchs, "High signal-to-noise ratio differential conductance spectroscopy," *J. Vac. Sci. Technol. B, Nanotechnol. Microelectron., Mater., Process., Meas., Phenomena*, vol. 39, no. 1, Jan. 2021, Art. no. 010601.

[22] H. Alemansour, S. O. R. Moheimani, J. H. G. Owen, J. N. Randall, and E. Fuchs, "Ultrafast method for scanning tunneling spectroscopy," *J. Vac. Sci. Technol. B, Nanotechnol. Microelectron., Mater., Process., Meas., Phenomena*, vol. 39, no. 4, Jul. 2021, Art. no. 042802.

[23] R. Mishra, N. Nikooienejad, S. O. Reza Moheimani, and I. R. Petersen, "Kalman filter based estimation of surface conductivity in STM," in *Proc. IEEE Conf. Control Technol. Appl. (CCTA)*, Aug. 2022, pp. 950–955.

[24] G. Besançon, A. Voda, and A. Popescu, "Closed-loop-based observer approach for tunneling current parameter estimation in an experimental STM," *Mechatronics*, vol. 83, May 2022, Art. no. 102743.

[25] F. Tajaddodianfar, S. O. R. Moheimani, and J. N. Randall, "Scanning tunneling microscope control: A self-tuning PI controller based on online local barrier height estimation," *IEEE Trans. Control Syst. Technol.*, vol. 27, no. 5, pp. 2004–2015, Sep. 2019.

[26] F. Tajaddodianfar, S. O. R. Moheimani, J. Owen, and J. N. Randall, "On the effect of local barrier height in scanning tunneling microscopy: Measurement methods and control implications," *Rev. Sci. Instrum.*, vol. 89, no. 1, Jan. 2018, Art. no. 013701.

[27] B. Voigtländer, *Scanning Probe Microscopy: Atomic Force Microscopy and Scanning Tunneling Microscopy*. Cham, Switzerland: Springer, 2015.

[28] Y. Kuk and P. J. Silverman, "Scanning tunneling spectroscopy of metal surfaces," *J. Vac. Sci. Technol. A, Vac., Surf., Films*, vol. 8, no. 1, pp. 289–292, Jan. 1990.

[29] F. Tajaddodianfar, A. Fowler, E. Fuchs, J. N. Randall, and S. O. R. Moheimani, "Frequency-domain closed-loop system identification of a scanning tunneling microscope," in *Proc. ASPE Spring Topical Meeting Precis. Mech. Syst. Design Control*, 2016, pp. 54–57.

[30] F. Tajaddodianfar, S. O. R. Moheimani, J. Owen, and J. N. Randall, "A self-tuning controller for high-performance scanning tunneling microscopy," in *Proc. IEEE Conf. Control Technol. Appl. (CCTA)*, Aug. 2017, pp. 106–110.

[31] M. G. Ruppert, D. M. Harcombe, M. R. P. Ragazzon, S. O. R. Moheimani, and A. J. Fleming, "A review of demodulation techniques for amplitude-modulation atomic force microscopy," *Beilstein J. Nanotechnol.*, vol. 8, pp. 1407–1426, Jul. 2017.

[32] A. Gelb et al., *Applied Optimal Estimation*. Cambridge, MA, USA: MIT Press, 1974.

[33] M. G. Ruppert, K. S. Karvinen, S. L. Wiggins, and S. O. Reza Moheimani, "A Kalman filter for amplitude estimation in high-speed dynamic mode atomic force microscopy," *IEEE Trans. Control Syst. Technol.*, vol. 24, no. 1, pp. 276–284, Jan. 2016.

[34] K. S. Karvinen, M. G. Ruppert, K. Mahata, and S. O. R. Moheimani, "Direct tip-sample force estimation for high-speed dynamic mode atomic force microscopy," *IEEE Trans. Nanotechnol.*, vol. 13, no. 6, pp. 1257–1265, Nov. 2014.

[35] D. Simon, *Optimal State Estimation: Kalman, H_∞, and Nonlinear Approaches*. Hoboken, NJ, USA: Wiley, 2006.

[36] M. S. Grewal and A. P. Andrews, *Kalman filtering: Theory and Practice with MATLAB*. Hoboken, NJ, USA: Wiley, 2014.

[37] J. G. Proakis, *Digital Signal Processing: Principles, Algorithms, and Applications, 4/E*. London, U.K.: Pearson, 2007.

[38] C. Woo Lee and C. Choo Chung, "Design of a new multi-loop disturbance observer for optical disk drive systems," *IEEE Trans. Magn.*, vol. 45, no. 5, pp. 2224–2227, May 2009.

[39] J. A. Butterworth, L. Y. Pao, and D. Y. Abramovitch, "Analysis and comparison of three discrete-time feedforward model-inverse control techniques for nonminimum-phase systems," *Mechatronics*, vol. 22, no. 5, pp. 577–587, 2012.

[40] [Online]. Available: https://www.zyvexlabs.com/apm/products/zyvector/

[41] A. Alipour, M. B. Coskun, and S. O. R. Moheimani, "A MEMS nanopositioner with integrated tip for scanning tunneling microscopy," *J. Microelectromech. Syst.*, vol. 30, no. 2, pp. 271–280, Apr. 2021.

[42] A. Alipour, S. O. R. Moheimani, J. H. G. Owen, E. Fuchs, and J. N. Randall, "Atomic precision imaging with an on-chip scanning tunneling microscope integrated into a commercial ultrahigh vacuum STM system," *J. Vac. Sci. Technol. B, Nanotechnol. Microelectron., Mater., Process., Meas., Phenomena*, vol. 39, no. 4, Jul. 2021, Art. no. 040603.

Richa Mishra received the B.S. degree in electrical engineering from the National Institute of Technology, Raipur, India, in 2007, and the M.S. degree in electrical engineering from IIT Bombay, Mumbai, India, in 2016. She is currently pursuing the Ph.D. degree with the Department of Electrical and Computer Engineering, The University of Texas at Dallas, Richardson, TX, USA.

Her research interests include atomic precise manufacturing with a scanning tunneling microscope (STM), application of advanced control in STM, control design, and signal processing.

S. O. Reza Moheimani (Fellow, IEEE) received the Ph.D. degree in electrical engineering from the University of New South Wales, Sydney, NSW, Australia, in 1996.

He is currently a Professor and holds the James Von Ehr Distinguished Chair in Science and Technology at the Department of Systems Engineering, The University of Texas at Dallas, Richardson, TX, USA, with appointments at the Department of Electrical and Computer Engineering and the Department of Mechanical Engineering. He is also the Founding Director of the UTD Center for Atomically Precise Fabrication of Solid-State Quantum Devices and the Founder and the Director of the Laboratory for Dynamics and Control of Nanosystems, The University of Texas at Dallas. His current research interests include applications of control and estimation in high-precision mechatronic systems, high-speed scanning probe microscopy, and atomically precise manufacturing.

Prof. Moheimani is a fellow of International Federation of Automatic Control (IFAC), American Society of Mechanical Engineers (ASME), and the Institute of Physics, U.K. He received the Industrial Achievement Award from IFAC in 2023, the Nyquist Lecturer Award from ASME DSCD in 2022, the Charles Stark Draper Innovative Practice Award from ASME DSCD in 2020, the Nathaniel B. Nichols Medal from IFAC in 2014, the IEEE Control Systems Technology Award from IEEE Control Systems Society (CSS) in 2009, and the IEEE TRANSACTIONS ON CONTROL SYSTEMS TECHNOLOGY Outstanding Paper Award from IEEE CSS in 2007 and 2018. He is a past Editor-in-Chief of *Mechatronics* from 2016 to 2021 and a past Associate Editor of IEEE TRANSACTIONS ON CONTROL SYSTEMS TECHNOLOGY, IEEE TRANSACTIONS ON MECHATRONICS, and *Control Engineering Practice*.